ERA5 deficit in supercooled liquid water cloud radiative forcing at Dome C, Antarctica

Philippe Ricaud

Received: 27 March 2025 | Revised: 20 August 2025 | Accepted: 21 August 2025

DOI: 10.1002/qj.70025

Quarterly Journal of the Royal Meteorological Society RMetS

RESEARCH ARTICLE

ERA5 deficit in supercooled liquid water cloud radiative forcing at Dome C, Antarctica

Philippe Ricaud

Météo-France, CNRS, Univ. Toulouse, CNRM, Toulouse, France

Correspondence
Philippe Ricaud, Météo-France, CNRS, Univ. Toulouse, CNRM, Toulouse, France.
Email: philippe.ricaud@meteo.fr

Abstract

Clouds play a crucial role in estimating Earth's climate evolution, with their impact depending on their composition whether they contain solid or liquid water. In Antarctica, clouds containing supercooled liquid water (SLW), which exists at temperatures below 0°C, are challenging to observe and often poorly represented in climate models. A recent observational study conducted at Dome C, Concordia station (75°06′ S, 123°21′ E, 3233 m altitude) on the Eastern Antarctic Plateau revealed a logarithmic relationship between liquid water path (LWP, liquid water profile integrated along the vertical) and SLW cloud radiative forcing (CRF) during summer (December 2018–2021). To assess whether this relationship holds over a longer period, we analysed meteorological reanalyses from ERA5 for December from 1940 to the present. Our analysis indicates that, during December 2018–2021, the ERA5 distribution of SLW CRF–LWP conforms to the observational relationship and remains within its domain of validity. ERA5 SLW CRF varies from 0 to a maximum of 55 $W \cdot m^{-2}$ when LWP varies from 0.1 to a maximum of 1.4 $g \cdot m^{-2}$. But the maximum of SLW CRF in ERA5 underestimates the observations by approximately −15 $W \cdot m^{-2}$ (∼20%) attributed to biases in long-wave downward SLW CRF (accounting for two-thirds of the deficit) and short-wave SLW CRF (one-third). Our study reveals a notable increase in summertime SLW clouds from the 1980s to the contemporary era with no significant change prior to the 1980s when the reanalysis data quality in the 1940s degrades. The increase of SLW clouds may be explained by the positive trend in maximum in-cloud temperatures (from −23°C in the 1940s to −18°C in the 2020s). Our findings emphasise the need for improved representation of SLW clouds in numerical weather prediction and climate models to enhance projections of climate evolution.

KEYWORDS

Antarctica, cloud radiative forcing, Concordia station, ERA5 reanalyses, liquid fog, supercooled liquid water

1 | INTRODUCTION

Clouds are among the most crucial factors regulating Earth's radiation balance, influencing both the energy reaching the surface and the heat escaping into space. They can either cool or warm the atmosphere and contribute to the water cycle through precipitation (Komurcu et al., 2014; Storelvmo, 2017; Tsushima et al., 2006). The composition of clouds – whether they contain liquid or solid water – also affects the global radiative budget and, consequently, Earth's climate (Choi et al., 2014; Lemus et al., 1997; Lenaerts et al., 2017).

In Antarctica, due to surface temperatures consistently well below freezing (0°C), clouds primarily consist of ice (Lachlan-Cope, 2010). However, over the past decade, satellite, airborne, and ground-based observations have revealed that a significant portion of Antarctic clouds also contain liquid water (Grosvenor et al., 2012; Lachlan-Cope et al., 2016; Silber et al., 2019b; Turner et al., 2007). This liquid water, when present at temperatures below 0°C, is referred to as supercooled liquid water (SLW). Theoretically, SLW can exist at temperatures ranging from 0°C to −39°C. SLW is typically scarce because ice crystals form and grow at the expense of liquid droplets through the Wegener–Bergeron–Findeisen process (Bergeron, 1928; Findeisen, 1938; Storelvmo & Tan, 2015; Wegener, 1911). Clouds containing both SLW and ice are classified as mixed-phase clouds.

Antarctica, one of the driest and coldest regions on Earth, has significantly less atmospheric water (in liquid, solid, or gaseous form) compared to tropical and mid-latitude regions. Despite this, Antarctic clouds play a key role in the climate system by influencing Earth's radiation balance – both locally at high southern latitudes and globally through complex teleconnections (Lubin et al., 1998). Cloud cover over Antarctica varies, with a fractional coverage of 80%–90% near the coast and about 50%–60% near the South Pole (Bromwich et al., 2012; Listowski et al., 2019). Mixed-phase clouds are more commonly observed near coastal areas, while ice clouds dominate the continent's interior (Listowski et al., 2019). Consequently, during summer, the frequency of SLW cloud occurrences decreases markedly from coastal regions (20%–30%) toward the pole (5%–10%), with substantially low cloud frequency over the Eastern Antarctic Plateau (5%–10%) compared to the Western Antarctic region (30%–40%) and the Antarctic Peninsula (40%–50%) (Listowski et al., 2019). From observations and climate models in Antarctica, the liquid water path (LWP), which is the vertically-integrated liquid water content, is on average less than 10 $g \cdot m^{-2}$, with slightly larger values in summer than in winter by 2–5 $g \cdot m^{-2}$ (Lenaerts et al., 2017). On average, coastal LWP (including the Antarctic Peninsula) is 10–20 $g \cdot m^{-2}$ greater than in the interior of the continent. In the Southern Ocean, LWP values range from 20 to 100 $g \cdot m^{-2}$ (Lenaerts et al., 2017). In the Arctic, LWP values from 50 to 100 $g \cdot m^{-2}$ were already reported (Lemus et al., 1997; Zhang et al., 2019) with much less amounts over Greenland (10–40 $g \cdot m^{-2}$). At middle/tropical latitudes, values ranging from 100 to 150 $g \cdot m^{-2}$ were measured and simulated (Lemus et al., 1997).

The optical properties of Antarctic clouds depend on the concentration and type of cloud condensation nuclei (CCN) and ice nucleating particles (INP), yet significant uncertainties remain regarding their origin and abundance over the continent. A major challenge is that both research and operational weather models struggle to accurately represent Antarctic clouds, particularly SLW clouds (McCoy et al., 2015; Wang et al., 2022). These inaccuracies result in significant biases – often exceeding several tens of watts per square metre ($W \cdot m^{-2}$) – in net surface irradiance across Antarctica and the Southern Ocean (Bodas-Salcedo et al., 2016; Bromwich et al., 2013; King et al., 2006, 2015; Lawson & Gettelman, 2014; Listowski & Lachlan-Cope, 2017; Young et al., 2019).

Dome C, Concordia station, located 1100 km inland at an elevation of 3233 m above sea level on the Antarctic Plateau, serves as a unique natural laboratory. With minimal atmospheric water content (approximately 1 mm of precipitable water in summer) and sufficiently low temperatures in December (summer) to observe SLW clouds between −38°C and −12°C (Ricaud et al., 2024), it provides an ideal setting for studying cloud dynamics. Additionally, its relatively uniform topography minimises small-scale influences on both observations and model outputs (Cossich et al., 2021; Ricaud et al., 2020a,b). This site is well suited for studying the impact of the SLW clouds on the surface radiative forcing (Ricaud et al., 2024).

The downward and upward long-wave (4 to 50 μm) and short-wave (0.3 to 3 μm) surface irradiances (F) define the net surface irradiance (F_{Net}). Consistent with the method presented in Ricaud et al. (2024), F_{Net} is calculated as the difference between the downward and upward components (Driemel et al., 2018) as:

$$F_{\mathrm{Net}} = \left(F_{\mathrm{LW}}^{\mathrm{Down}} - F_{\mathrm{LW}}^{\mathrm{Up}}\right) + \left(F_{\mathrm{SW}}^{\mathrm{Down}} - F_{\mathrm{SW}}^{\mathrm{Up}}\right), \qquad (1)$$

where $F_{\mathrm{LW}}^{\mathrm{Down}}$, $F_{\mathrm{LW}}^{\mathrm{Up}}$, $F_{\mathrm{SW}}^{\mathrm{Down}}$, and $F_{\mathrm{SW}}^{\mathrm{Up}}$ represent the downward long-wave, upward long-wave, downward short-wave and upward short-wave surface irradiances, respectively. At a given time, the impact of a cloud on the surface irradiance is estimated from the difference between the net irradiance, in cloudy ($F_{\mathrm{Net,cld}}$) and cloud-free (FCF_{Net}) conditions (Stapf et al., 2020) to provide the so-called 'cloud

radiative forcing' (CRF) ΔF_{Net}:

$$\Delta F_{\text{Net}} = F_{\text{Net,cld}} - FCF_{\text{Net}}. \quad (2)$$

A similar equation can be written for each of the four irradiances that appear in the right-hand side of Equation (1).

Recent surface-based observations at the Concordia station (75°06′ S, 123°21′ E) in summer have provided valuable insights into SLW clouds (Ricaud et al., 2024). These observations revealed a logarithmic relationship between in-cloud temperature and LWP. A logarithmic relationship is also found between SLW CRF and LWP. These findings offer a valuable tool for assessing the accuracy of meteorological and climate models in simulating clouds and their associated radiative effects.

We have utilised these published datasets to evaluate the accuracy of the state-of-the-art reanalysis data provided by the European Centre for Medium-Range Weather Forecasts (ECMWF), specifically the ECMWF Reanalysis v5 (ERA5). ERA5 (Hersbach et al., 2020; Soci et al., 2024) represents the fifth generation of ECMWF's atmospheric reanalysis, covering global climate data from January 1940 to the present (Bell et al., 2021). Its meteorological parameters, such as near-surface air temperature and wind, have already been validated over the western part of Antarctica (Tetzner et al., 2019). The mean bias between ERA5 reanalyses and observations in Eastern Antarctica during summer (DJF) is about 1.5°C from 1979 to 2018 (Zhu et al., 2021). The Eastern Antarctic bias is consistent with the positive bias in the lowermost troposphere from the Météo-France NWP ARPEGE and AROME models compared balloon-borne and drone-borne in situ observations (Ricaud et al., 2023).

The present study pursues three main objectives:

1. to validate the relationship between LWP and SLW CRF in ERA5 reanalysis data using observational datasets;
2. to identify and assess potential sources of bias in the ERA5 dataset; and
3. to investigate the long-term temporal evolution of the LWP–SLW CRF relationship within ERA5.

The article is organised as follows: Section 2 details the datasets used in our study while Section 3 details the methodology. Section 4 presents and discusses the SLW CRFs derived from ERA5. In Section 5, we examine the contributions of long-wave and short-wave surface radiation to SLW CRFs. Section 6 explores the effects of surface albedo on SLW CRF, the in-cloud temperature sensitivity to SLW and ice clouds, the presence of liquid fog and the diurnal variation of SLW clouds in ERA5. Finally, Section 7 provides the study's conclusions.

2 | DATASETS

2.1 | ERA5

ERA5 provides a set of variables encompassing the net and downward long-wave, and the net and downward short-wave surface irradiances in cloudy (if any clouds are present) and cloud-free conditions on an hourly rate from 1940 to date, at a horizontal resolution of 0.25° × 0.25°. ERA5 also gives LWP (SLW total columns), and IWP (ice total columns) and, along the vertical, temperature, ice water content (IWC) and liquid water cloud content (LWC). The clouds generated in ERA5 have two regimes: (1) below −38°C where homogeneous freezing occurs (only ice crystals), and (2) between −38°C and 0°C, where mixed-phase (liquid and solid) clouds can occur (Forbes & Ahlgrimm, 2014). For temperatures greater than −38°C when SLW and ice coexist, they are assumed to be well mixed and distributed uniformly through the cloud.

For our analysis, the latitudes selected in ERA5 are: 75.00° S, 75.25° S and 75.50° S; and the selected longitudes are: 123.00° E, 123.25° E and 123.50° E, giving nine points encompassing the location of the Concordia station (see Figure 1). Note that the nine points are not centred with respect to the station but displaced southward to account for the climatological northward winds. The ERA5 data are provided every hour. Knowing that the surface pressure in summer at the Concordia station is about 650 hPa, we have selected the 13 following levels: 150, 175, 200, 225, 250, 300, 350, 400, 450, 500, 550, 600, and 650 hPa. Note that, at the Concordia station, SLW clouds are usually observed at heights less than 2000 m above ground level (agl), approximate pressure ranging from 480 to 495 hPa, in December 2018–2021. The ERA5 variables used in our study are presented in Table 1.

We considered that a SLW or ice cloud was present in the ERA5 dataset when the total column supercooled liquid water (tcslw) or total column cloud ice water (tciw) was greater than 0, respectively. The different components of the SLW CRF were calculated as follows:

$$\Delta F_{\text{Net}} = (\text{ssr} - \text{ssrc}) + (\text{str} - \text{strc}), \quad (3)$$

$$\Delta F_{\text{LW}}^{\text{Down}} = \text{strd} - \text{strdc}, \quad (4)$$

$$\Delta F_{\text{SW}}^{\text{Down}} = \text{ssrd} - \text{ssrdc}, \quad (5)$$

$$\Delta F_{\text{LW}}^{\text{Up}} = \Delta F_{\text{LW}}^{\text{Down}} - (\text{str} - \text{strc}), \quad (6)$$

$$\Delta F_{\text{SW}}^{\text{Up}} = \Delta F_{\text{SW}}^{\text{Down}} - (\text{ssr} - \text{ssrc}). \quad (7)$$

In Section 3 *Methodology*, we will consider four periods in the ERA5 datasets:

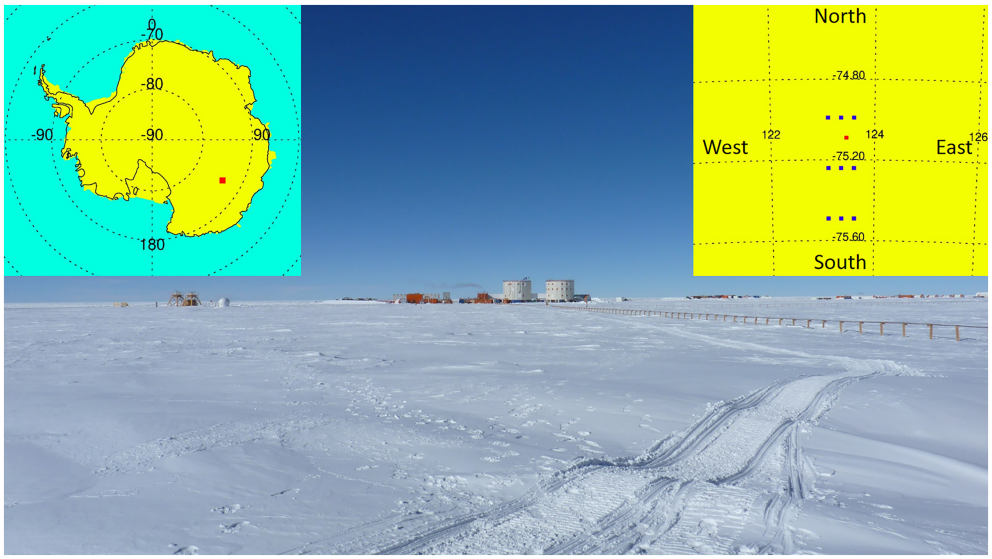

FIGURE 1 Picture of the Concordia (Dome C) station taken from the South with its location (red filled square highlighted in the Antarctic continent [yellow area] surrounded by the Southern Ocean [blue area]) presented in the top left hand side insert in the picture. The locations of the nine outputs from ERA5 (filled blue squares) together with the location of the Concordia station (red filled square) are depicted on the top right-hand side insert in the picture. [Colour figure can be viewed at wileyonlinelibrary.com]

TABLE 1 List of the ERA5 variables, definitions and units used in our analysis.

ERA5 variables	Definition	Units	Units used in our study
2D fields			
ssr	Surface net short-wave (solar) radiation	$J \cdot m^{-2}$	$W \cdot m^{-2}$
ssrc	Surface net short-wave (solar) radiation, clear sky	$J \cdot m^{-2}$	$W \cdot m^{-2}$
str	Surface net long-wave (thermal) radiation	$J \cdot m^{-2}$	$W \cdot m^{-2}$
strc	Surface net long-wave (thermal) radiation, clear sky	$J \cdot m^{-2}$	$W \cdot m^{-2}$
ssrd	Surface short-wave (solar) radiation downward	$J \cdot m^{-2}$	$W \cdot m^{-2}$
ssrdc	Surface solar radiation downward, clear sky	$J \cdot m^{-2}$	$W \cdot m^{-2}$
strd	Surface long-wave (thermal) radiation downward	$J \cdot m^{-2}$	$W \cdot m^{-2}$
strdc	Surface thermal radiation downward, clear sky	$J \cdot m^{-2}$	$W \cdot m^{-2}$
tciw (IWP)	Total column cloud ice water	$kg \cdot m^{-2}$	$g \cdot m^{-2}$
tcslw (LWP)	Total column supercooled liquid water	$kg \cdot m^{-2}$	$g \cdot m^{-2}$
3D fields			
t	Temperature	K	°C
clwc (LWC)	Specific cloud liquid water content	$kg \cdot kg^{-1}$	$g \cdot m^{-3}$
ciwc (IWC)	Specific cloud ice water content	$kg \cdot kg^{-1}$	$g \cdot m^{-3}$

a. P1: December 1943–1952 (beginning of the ERA5 dataset)
b. P2: December 1983–1992 (middle of the ERA5 dataset)
c. P3: December 2013–2022 (contemporary era, end of the ERA5 dataset)
d. P4: December 2018–2021 (period consistent with the observational dataset from Ricaud et al., 2024). Please note, P3 encompasses P4

First, we will focus our analysis on the period covered by the observational dataset from Ricaud et al. (2024), specifically December 2018–2021, named period P4. This period allows for a direct comparison between ERA5 SLW CRF and observed SLW CRF. Second, we will divide the available ERA5 dataset into three arbitrarily chosen 10-year periods, namely periods P1, P2 and P3.

An uncertainty estimate is sampled by an underlying 10-member ensemble at three-hourly intervals. Such uncertainty estimates are closely related to the information content of the available observing system which has evolved considerably over time. The uncertainty estimates in ERA5 mostly account for random errors and not for systematic ones. As an example, the number of observations assimilated increases from 53,000 per day in early 1950 to 570,000 per day by the end of 1978. Accordingly, the quality of the reanalysis improves throughout the period,

TABLE 2 Mean spread, namely the standard deviation around the ensemble mean, of the ERA5 variables used in our analysis over the periods P1 to P3.

Period	P1: 1943–1952	P2: 1983–1992	P3: 2013–2022
Temperature @ 650 hPa (K)	2.79	0.42	0.26
tcslw ($kg{\cdot}m^{-2}$) $\times 10^{-5}$	5.00	5.33	5.37
ssr ($W{\cdot}m^{-2}$)	13.39	4.19	4.18
ssrc ($W{\cdot}m^{-2}$)	2.03	0.42	0.18
str ($W{\cdot}m^{-2}$)	36.60	10.42	9.06
strc ($W{\cdot}m^{-2}$)	14.03	3.63	2.41

generally joining seamlessly with the segment covering 1979 to the present (Bell et al., 2021).

We present in Table 2 the mean spread, namely the standard deviation around the ensemble mean, within the 10-member ensemble of the ERA5 variables used in our analysis (temperature at 650 hPa, LWP and net surface thermal and solar radiations including clear-sky radiations) over the periods P1, P2 and P3 (P4 is included in P3). If we consider the ERA5 temperature spread at 650 hPa, we see that the spread greatly diminishes from P1 (2.79 K) to P2 (0.42 K) and slightly lessens in P3 (0.26 K). Regarding LWP (tcslw ERA5 variable), the spread is rather stable over the three periods (0.0500–0.0537 $g{\cdot}m^{-2}$). The spread in the net surface radiations always diminishes from P1 to P3: solar (from 13.39 to 4.18 $W{\cdot}m^{-2}$), solar clear sky (from 2.03 to 0.18 $W{\cdot}m^{-2}$), thermal (from 36.60 to 9.06 $W{\cdot}m^{-2}$) and thermal clear sky (from 14.03 to 2.41 $W{\cdot}m^{-2}$).

2.2 | Observations

In our analysis, we have also used observations from different instruments installed at the Concordia station and we have treated them in such a way that it has been possible to estimate the SLW CRF. From the main results presented in Ricaud et al. (2024), we can summarise the following key points. Observations of LWP and in-cloud temperature were performed by a ground-based microwave radiometer HAMSTRAD (H_2O Antarctica Microwave Stratospheric and Tropospheric Radiometers) operating at 60 and 183 GHz. Observations of SLW clouds were deduced from the depolarisation ratio measured by a ground-based aerosol lidar (Light Detection And Ranging) operating at 532 nm by selecting values less than 10%. Downward and upward broadband short-wave (0.3–3 μm) and long-wave (4–50 μm) surface radiations were observed by instruments operated within the international Baseline Surface Radiation Network (BSRN). Coincident observations were treated over four months of December from 2018 to 2021 (the period P4).

As it is impossible to obtain simultaneously observations in cloud-free conditions together with SLW clouds, we developed a methodology to estimate cloud-free radiation when SLW clouds are observed. A parameterisation of the cloud-free downward long-wave (Dupont et al., 2008) and short-wave (Dutton et al., 2004) surface radiations widely used in the community has thus been applied to our measurements. The cloud-free upward short-wave radiation was estimated from both the cloud-free downward short-wave radiation and the surface albedo measured by BSRN instruments. The cloud-free upward long-wave radiation was estimated from the cloud-free downward long-wave radiation, the measured surface temperature and the surface emissivity assumed constant and equal to 0.99.

Regarding the errors and given the large number of observations used per 5 $W{\cdot}m^{-2}$ bins (1000–3000), it was estimated that the random error on the weighted-average radiations was negligible (0.3–0.7 $W{\cdot}m^{-2}$) whatever the short-wave or long-wave radiations considered. The bias in temperature is 0 to 2°C below 100 m agl and between −2 and 0°C between 100 and 1000 m agl with a negligible random error on the weighted-average temperature (<0.02°C). For LWP, the random error on the weighted-average LWP is less than 0.08 $g{\cdot}m^{-2}$. Based on clear-sky observations, a positive bias can be estimated to be of the order of 0.4 $g{\cdot}m^{-2}$.

Another source of error comes from (1) the geometry of observation and (2) the discontinuous SLW cloud layer. Firstly, lidar is almost zenith-pointing, HAMSTRAD makes a scan in the easterly direction (from 10° elevation to zenith), whilst the BSRN radiometers detect the radiation in a 2π-steradians field of view (3D configuration). That is to say, in our analysis, the whole sky contributes to the radiation whilst only the cloud at zenith (1D configuration) and in the easterly direction (2D configuration) is observed by the lidar and HAMSTRAD, respectively. Secondly, SLW clouds cannot be considered as uniform in the whole.

Lidar observations of SLW clouds have been time- and vertically interpolated onto the HAMSTRAD time sampling and vertical retrieval grid, respectively. The BSRN radiances have been time-interpolated onto the HAMSTRAD time sampling. Note that HAMSTRAD, lidar and BSRN observations were not assimilated in the ECMWF system providing ERA5 reanalyses.

TABLE 3 Bin width associated to the different ERA5 variables used in our statistical analysis.

Variables	Bin width	Unit
In-cloud temperature (T)	1.0	°C
LWP	0.2	$g{\cdot}m^{-2}$
IWP	0.2	$g{\cdot}m^{-2}$
LWC	0.001	$g{\cdot}m^{-3}$
IWC	0.001	$g{\cdot}m^{-3}$
SLW CRF (ΔF)	5.0	$W{\cdot}m^{-2}$

Abbreviations: CRF, cloud radiative forcing; IWC, ice water content; IWP, ice water path; LWC, liquid water content; LWP, liquid water path; SLW, supercooled liquid water.

TABLE 4 Offset in LWP (Δ_{LWP}) associated with the new function f_2(LWP) depending on the variable considered.

Variables	Offset (Δ_{LWP})/$g{\cdot}m^{-2}$
In-cloud temperature (T)	0.71
ΔF_{net}	1.30
ΔF_{LW}^{Down}	0.93
ΔF_{LW}^{Up}	0.0
ΔF_{SW}^{Down}	1.26
ΔF_{SW}^{Up}	1.31

3 | METHODOLOGY

Consistent with the statistical method used for observations (Ricaud et al., 2024), the ERA5 datasets associated with the four periods (P1–P4) are binned according to the Table 3. The number of points per bin is calculated for all paired datasets (X, Y) with X = LWP, IWP, LWC and IWC and $Y = T$ and ΔF. Note that we consider all the components of ΔF (ΔF_{net}, ΔF_{LW}^{Down}, ΔF_{LW}^{Up}, ΔF_{SW}^{Down} and ΔF_{SW}^{Up}).

The 2D probability density (PD) is calculated for the paired datasets and defined as $PD_{ij} = 100\,\frac{N_{ij}}{N_t}$, where N_{ij} and N_t are the count number in the bin ij and the total count number ($N_t = \sum_{j=1}^{L}\sum_{i=1}^{M} N_{ij}$), respectively, with M and L being the total number of bins in X and in Y, respectively. For each value of Y_j, a weighted average of X ($\overline{X_j}$) is calculated together with its associated weighted standard deviation (σ_{X_j}), considering all the X_{ij} values from $i = 1$ to M, with M the total number of X bins as:

$$\overline{X_j} = \frac{\sum_{i=1}^{M} N_{ij}\, X_{ij}}{\sum_{i=1}^{M} N_{ij}} \tag{8}$$

and

$$\sigma_{X_j} = \sqrt{\frac{\sum_{i=1}^{M} N_{ij}\left(X_{ij} - \overline{X_j}\right)^2}{\sum_{i=1}^{M} N_{ij}}} \tag{9}$$

In general, and contrarily to the method used for the observations, for the Y dataset (T and ΔF), the distribution of the total count numbers N_{tj} ($N_{tj} = \sum_{i=1}^{M} N_{ij}$ with $j = 1, \ldots, L$) cannot be fitted by any function $N(x)$ (see Figures S2–S6). For each value of Y_j, we have considered that the associated standard deviation σ_{X_j} was corresponding to the random error of one single point in the bin and that the random error on the average δ_{X_j} was then calculated (Bevington & Robinson, 2003) as:

$$\delta_{X_j} = \sigma_{X_j}/\sqrt{N_{tj}}. \tag{10}$$

We systematically represent $\pm\,\delta_{X_j}$ on each of the Figures 2, 3, 5 and 6 below. In order to highlight the averaged data $\overline{X_j}$ with a sufficiently high number of points, we have shown them only when:

$$N_{tj}/N_{Max} > \varepsilon, \tag{11}$$

where $N_{Max} = \max(N_{tj})$ with $j = 1, \ldots, N$; and ε is a threshold value arbitrarily set to 3% (values from 2% to 5% do not change the results significantly).

From observations (Ricaud et al., 2024), LWP adheres to a logarithmic relationship f_1(LWP) with both in-cloud temperature and SLW CRF described by the equation:

$$f_1(\mathrm{LWP}) = (\alpha \pm \delta\alpha) + \beta\ \ln(\mathrm{LWP}), \tag{12}$$

where α, $\delta\alpha$ and β are constants. $\delta\alpha$ corresponds to the range of α values where the relationship is valid, namely the domain of validity of the relationship. In the observations, LWPs never reach the null value because of a positive bias. Therefore, we have applied an offset in LWP (Δ_{LWP}) to ensure that LWP $\equiv 0$, producing a new function f_2(LWP):

$$f_2(\mathrm{LWP}) = f_1(\mathrm{LWP} + \Delta_{LWP}). \tag{13}$$

Table 4 presents the values of Δ_{LWP} used for the new function f_2(LWP). From now, we will always use the function f_2(LWP) to compare with the ERA5 datasets in P4.

4 | SUPERCOOLED LIQUID WATER CLOUD RADIATIVE FORCING

Considering the contemporary period P4, the probability density of the SLW CRF (ΔF_{net}) as a function of LWP calculated with the ERA5 data is presented Figure 2a.

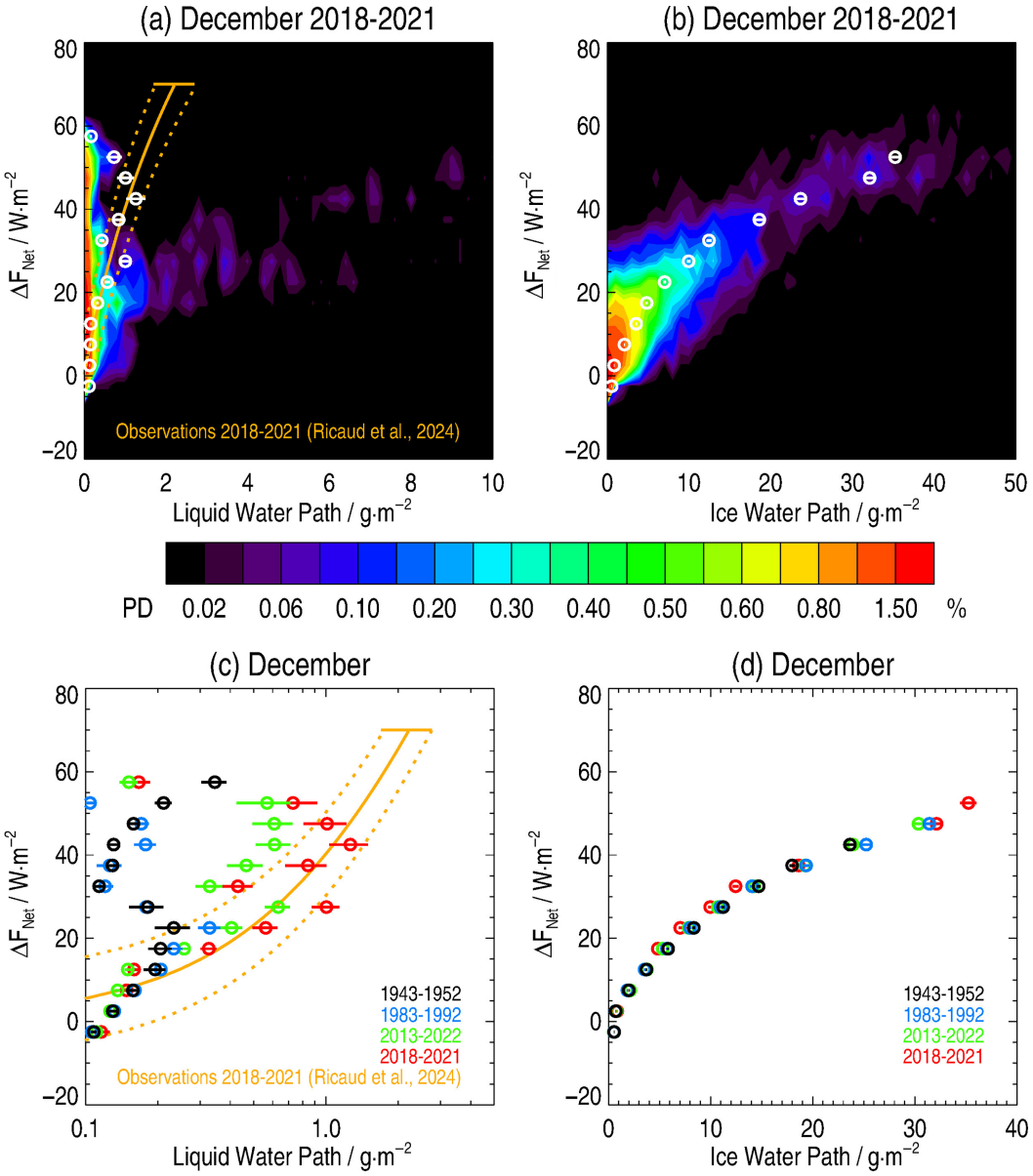

FIGURE 2 (a) Probability density (PD, %) of the supercooled liquid water (SLW) cloud radiative forcing (CRF) (ΔF_{net}, W·m^{-2}) as a function of liquid water path (LWP, g·m^{-2}) calculated from ERA5 reanalyses during December 2018–2021 at Concordia station, Antarctica. Also represented are the weighted-average LWPs within each 5-W·m^{-2} bin in SLW CRF (white circles) with a horizontal bar showing the random error ($\pm\delta_{LWP}$) on the liquid water LWP mean (see Section 3 for the details of the method employed). (b) As in panel a but for ice water path (g·m^{-2}). (c) As in panel a but during four periods: 1943–1952 (black circles, P1); 1983–1992 (blue circles, P2); 2013–2022 (green circles, P3) and 2018–2021 (red circles, P4). (d) As in panel b but during the four periods shown in panel c. A logarithmic function (orange solid) with its domain of validity (within the two dashed orange lines) derived from unbiased observations performed at Concordia station in P4 is superimposed in panels a and c. [Colour figure can be viewed at wileyonlinelibrary.com]

Superimposed are the logarithmic relationship and its domain of validity from the debiased observations (new function f_2(LWP)). ERA5 SLW CRF increases from 0.0 to a maximum of 52.5 W·m^{-2} when LWP varies from 0.1 to a maximum of 1.4 g·m^{-2}. Note the LWP value of 1.4 g·m^{-2} corresponds to the SLW CRF of 42.5 W·m^{-2} (bin of 40.0–45.0 W·m^{-2}) while the SLW CRF value of 52.5 W·m^{-2} (bin of 50.0–55.0 W·m^{-2}) corresponds to a LWP value of 0.75 g·m^{-2}. On average, the ERA5 distribution aligns with the observational relationship remaining within its domain of validity. At elevated SLW CRFs (52.5 W·m^{-2}), the relationship between SLW CRF and LWP apparently tends to be lost (LWP ~ 0.75 ± 0.25 g·m^{-2}) probably because the number of significant points also tends to minimise (see Figure S2a) but still remains within its domain of validity.

The great majority of the ERA5 points do not show any sensitivity in LWP (less than 0.2 g·m^{-2} in LWP from 0 to 50 W·m^{-2} in SLW CRF). However, a subset of points tends to emphasise elevated values of LWP and increases as SLW CRF: from 1.0 to 10.0 g·m^{-2} in LWP with SLW CRF from 10.0 to 50.0 W·m^{-2}. The maximum in ERA5 SLW CRF is less than the maximum in observed SLW CRF by approximately 15.0 W·m^{-2}. The observed SLW CRF maximum is 67.5 W·m^{-2} (centre of the 65–70 W·m^{-2} bin) while the ERA5 SLW CRF maximum only reaches 52.5 W·m^{-2} (centre of the 50–55 W·m^{-2} bin).

Associated with the SLW clouds, ERA5 calculates the presence of ice (solid water) clouds reaching a maximum ice water path (IWP, ice content integrated along the vertical) of 35 g·m^{-2} for a maximum ΔF_{net} of 52.5 W·m^{-2} (Figure 2b). This means that ERA5 can also produce mixed-phased clouds, a mixture of liquid and solid water. Note that all the statistics related to the number of counts per bin and the associated standard deviation per bin are available in the Data S1.

If we now consider the three periods P1-3 (Figure 2c), we see that ΔF_{net} increases from 0.0 to approximately 20.0 W·m^{-2} with the LWPs increasing from 0.0 to 0.2–0.3 g·m^{-2}. For the two periods P1 (1943–1952) and P2 (1983–1992), ΔF_{net} increases to a maximum of 57.5 W·m^{-2} with no relationship with LWP. For the contemporary period P3 (2013–2022), ΔF_{net} continues increasing to a maximum of 52.5 W·m^{-2} with LWPs increasing to a maximum of 0.6 g·m^{-2}. Note that, in P3, the ΔF_{net} – LWP relationship is on the lower edge of the domain of validity.

Whatever the period considered, the maximum ERA5 SLW CRF following the empirical relationship does not exceed 52.5 W·m^{-2}, meaning that the ERA5 deficit in SLW CRF reaches −15 W·m^{-2} with respect to observational data. It is interesting to note that there is no significant change in ΔF_{net} – LWP between the P1 and P2 periods, and that a net increase in LWP is detected between P1–P2 and P3–P4 of about 0.6 g·m^{-2}, reaching a maximum in P4 (0.3 g·m^{-2} more LWP in P4 than in P3). We will investigate in the next sections what are the causes of this LWP increase.

The IWP associated with the presence of SLW clouds from P1 to P3 shows the same relationship ΔF_{net} – IWP as over the period P4 with slightly less IWP (1–2 g·m^{-2}) in P4 compared to the other periods (Figure 2d). This suggests that the phase partitioning favours liquid water over ice during the contemporary period P4. However, again, the SLW CRF does not exceed 52.5 W·m^{-2} whatever the period considered. It is thus crucial to quantify the origins of the −15 W·m^{-2} deficit in SLW CRF evaluated with ERA5 compared to the observations.

5 | LONG-WAVE AND SHORT-WAVE COMPONENTS OF CLOUD RADIATIVE FORCING

It is known (Ricaud et al., 2024; Silber et al., 2019a) that the estimation of the long-wave downward ($\Delta F_{\text{LW}}^{\text{Down}}$) component of ΔF_{net} affects primarily the calculation of the SLW CRF because (1) the long-wave upward ($\Delta F_{\text{LW}}^{\text{Up}}$) component does not depend on LWP (see Figures S1 and S2) the short-wave downward ($\Delta F_{\text{SW}}^{\text{Down}}$) and upward ($\Delta F_{\text{SW}}^{\text{Up}}$) components almost cancel out. Depending on the four periods, we have thus considered the sensitivity of $\Delta F_{\text{LW}}^{\text{Down}}$, $\Delta F_{\text{SW}}^{\text{Down}}$ and $\Delta F_{\text{SW}}^{\text{Up}}$ to LWP and IWP (Figure 3a–f).

The $\Delta F_{\text{LW}}^{\text{Down}}$ – LWP relationship in ERA5 follows the empirical function to a maximum of 30 W·m^{-2} in P1 and P2, up to 77.5 W·m^{-2} in P3 and P4 with 0.6 g·m^{-2} more liquid water in P4 (maximum of 1.6 g·m^{-2}) than in P3 (Figure 3a). There is a deficit of −10 W·m^{-2} between the ERA5 and the observational maximum of $\Delta F_{\text{LW}}^{\text{Down}}$. It has already been stated (Silber et al., 2019a) that ERA5, over Western Antarctica, tended to underestimate the downward long-wave surface radiation during clear-sky conditions by approximately 15 W·m^{-2} and during any type of cloud occurrence by 15–40 W·m^{-2}, most likely caused by a liquid water-deficient atmosphere. Regarding the short-wave components, the $\Delta F_{\text{SW}}^{\text{Down}}$ – LWP (Figure 3c) and $\Delta F_{\text{SW}}^{\text{Up}}$ – LWP (Figure 3e) in ERA5 follow the empirical function to a maximum of −50 W·m^{-2} in P1 and P2, up to −132.5 and −112.5 W·m^{-2}, respectively in P3 and P4 with 0.5 g·m^{-2} more liquid water in P4 (maximum of 1.5 g·m^{-2}) than in P3. But, considering the maxima of the components, there is still a difference compared to observations reaching +15 and + 20 W·m^{-2} in $\Delta F_{\text{SW}}^{\text{Down}}$ and $\Delta F_{\text{SW}}^{\text{Up}}$, respectively. Consequently, the deficit in the maximum of SLW CRF (−15 W·m^{-2}) can be attributed for two-thirds to the long-wave downward component (−10 W·m^{-2}) and for one-third to the short-wave component (15–20 = −5 W·m^{-2}).

The relationships $\Delta F_{\text{LW}}^{\text{Down}}$-, $\Delta F_{\text{SW}}^{\text{Down}}$-, and $\Delta F_{\text{SW}}^{\text{Up}}$ – IWP associated with the presence of SLW clouds do not exhibit large differences from P1 to P4 with slightly less IWP (1–2 g·m^{-2}) in P4 compared to the other periods (Figure 3b,d,f). This further suggests that the phase partitioning favours liquid water over ice during the contemporary period P4. Whatever the period considered, the three components of the SLW CRF do not exceed 67.5 W·m^{-2} for $\Delta F_{\text{LW}}^{\text{Down}}$, −77.5 W·m^{-2} for $\Delta F_{\text{SW}}^{\text{Down}}$ and −62.5 W·m^{-2} for $\Delta F_{\text{SW}}^{\text{Up}}$, that is to say largely less by about 20 W·m^{-2} than the maximum observed in the three components.

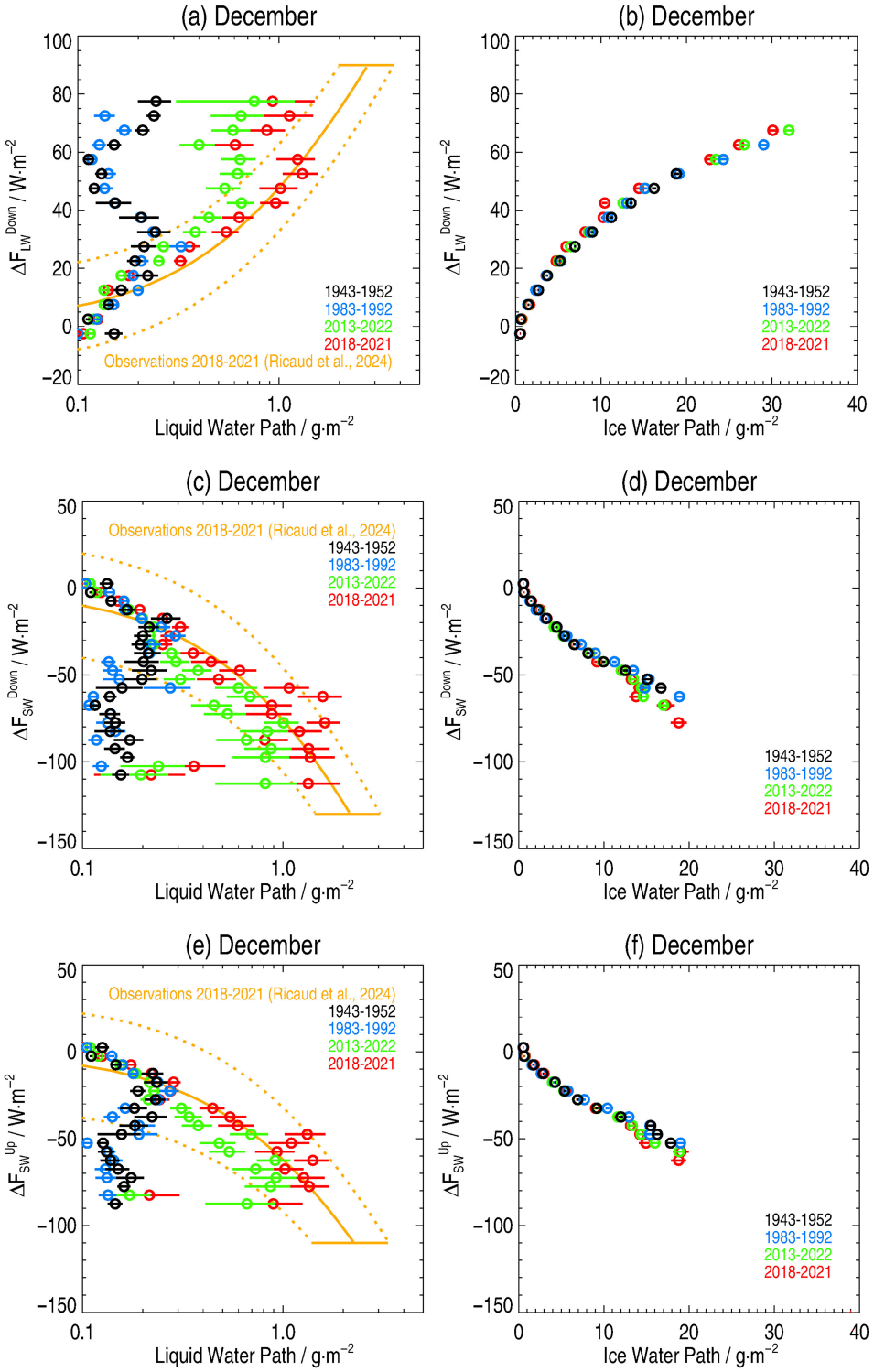

FIGURE 3
Weighted-average liquid water paths (LWPs) (g·m^{-2}) within each 5-W·m^{-2} bin in the three components of the supercooled liquid water (SLW) cloud radiative forcing (CRF) (W·m^{-2}): (a) ΔF_{LW}^{Down}, (c) ΔF_{SW}^{Down} and (e) ΔF_{SW}^{Up} with an horizontal bar showing the random error ($\pm\delta_{LWP}$) on the LWP mean calculated from ERA5 reanalyses at Concordia station, Antarctica during four periods: 1943–1952 (black circles, P1); 1983–1992 (blue circles, P2); 2013–2022 (green circles, P3) and 2018–2021 (red circles, P4). Weighted-average ice water profiles (IWPs, g·m^{-2}) within each 5-W·m^{-2} bin in the three components of the SLW CRF (W·m^{-2}): (b) ΔF_{LW}^{Down}, (d) ΔF_{SW}^{Down} and (f) ΔF_{SW}^{Up} with an horizontal bar showing the random error ($\pm\delta_{IWP}$) on the IWP mean calculated from ERA5 reanalyses at Concordia station, Antarctica during the four periods P1–P4. A logarithmic function (orange solid) with its domain of validity (within the two dashed orange lines) derived from unbiased observations performed at Concordia station in P4 is superimposed for the three components in panels a, c and e. [Colour figure can be viewed at wileyonlinelibrary.com]

6 | DISCUSSION

6.1 | Surface albedo effects

The maximum of the short-wave upward component of the SLW CRF (ΔF_{SW}^{Up}) shows a large difference with the maximum of the observations (20 W·m^{-2}). As described in Section 2, the short-wave upward surface irradiance F_{SW}^{Up} is evaluated from short-wave downward surface irradiance F_{SW}^{Down} via the surface albedo A ($A = F_{SW}^{Up}/F_{SW}^{Down}$). Ice surface albedo is usually very high (0.8) but, at the Concordia station, although the surface is constituted of ice, a non-negligible diurnal variation of A has been already observed and fitted, with an amplitude varying from 0.71 to 0.87 in cloud-free conditions (Ricaud et al., 2024). The observed diurnal variation of the surface albedo has been

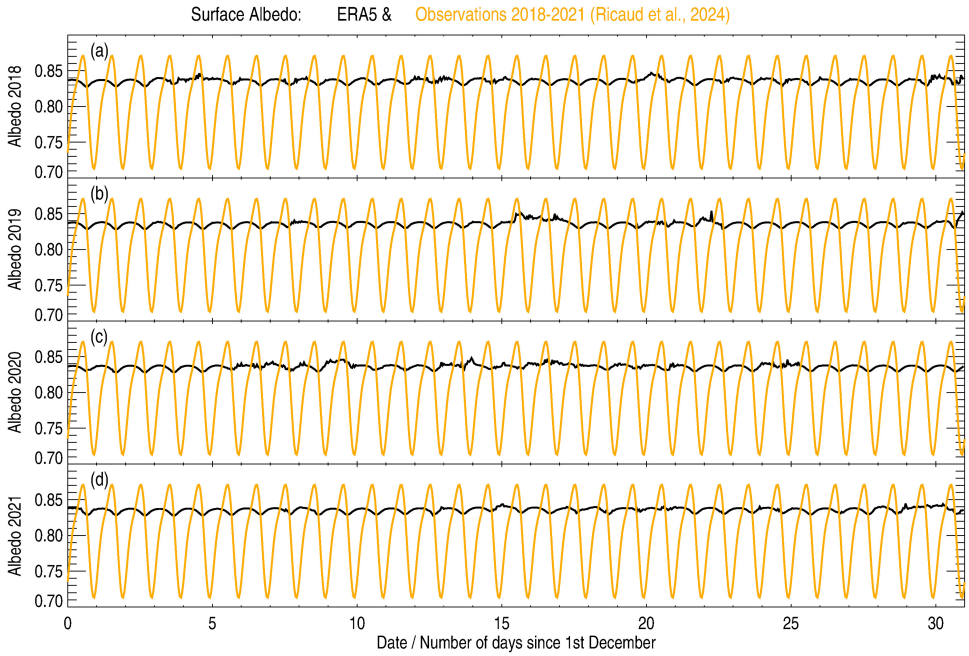

FIGURE 4 Time evolution of the surface albedo at Concordia station, Antarctica calculated by ERA5 (black) and cloud-free surface albedo fitted from observations (orange) in December 2018–2021 over the month of December (a) 2018, (b) 2019, (c) 2020 and (d) 2021. [Colour figure can be viewed at wileyonlinelibrary.com]

attributed to (1) the sastrugi (features formed by erosion of snow by wind) orientation and (2) the sun zenith angle which impacts on the surface albedo even with a flat snow surface (Gardner & Sharp, 2010). In P4, whatever the year considered (Figure 4), the amplitude of the ERA5 surface albedo variability is weak (0.02) varying from 0.83 to 0.85 whatever the conditions encountered (cloud-free or not). Reducing the surface albedo from 0.83 to a minimum of 0.71 in the ERA5 datasets (Figure 2c,e) will lead to less negative ΔF_{SW}^{Up} by a maximum of 12% thus more negative $\Delta F_{SW}^{Down} - \Delta F_{SW}^{Up}$ by about 5–10 $W \cdot m^{-2}$. In that configuration (surface albedo of 0.71), the deficit in ΔF_{net} will be even larger than the one estimated with a surface albedo of 0.83.

6.2 | In-cloud temperature sensitivity

We can verify now whether the presence of SLW in the contemporary period is related to an expected positive temperature trends from P1 to P4 over 80 years, namely the so-called global warming. From observations in P4, it has been shown that in-cloud temperature is logarithmically increasing with LWP from −36°C to −16°C for LWP varying from 1.0 to 14.0 $g \cdot m^{-2}$. In theory, SLW cannot persist below a temperature threshold of −39°C (Goy et al., 2018; Sippola & Taskinen, 2018).

If we now consider the four periods (P1–P4) covering 80 years from 1940 to the contemporary era, we can separate the evolution of in-cloud temperature–LWP (Figure 5a,c) into two domains for temperatures less or greater than a threshold value we have arbitrarily fixed to −23°C. In the contemporary era (P3 and P4), the ERA5 in-cloud temperature–LWP evolution follows the observational function with low LWPs (0.1–0.3 $g \cdot m^{-2}$) at temperatures around −35°C and high LWPs (5–13 $g \cdot m^{-2}$) at temperatures around −23°C to −18°C. But in a domain from −25°C to −33°C, LWPs are rather stable (0.1–0.3 $g \cdot m^{-2}$) with no temperature sensitivity. During the past periods (P1 and P2), in-cloud temperatures are less than −23°C and LWPs are weak (0.1–0.2 $g \cdot m^{-2}$) and do not show any temperature sensitivity, thus do not follow the observational function. Note that LWP during P3 (2013–2022) is strictly equal to LWP during P4 (2018–2021) for temperatures greater than −23°C because episodes of elevated in-cloud temperatures only happened during P4.

When SLW clouds are present, whatever the period considered, the evolution of the in-cloud temperature–IWP relationship (Figure 5b,d) is also highlighting two regimes for temperature less or greater than −23°C. IWP increases with temperature from −39°C (IWP varying 0.0–2.0 $g \cdot m^{-2}$) to −23°C (IWP varying 8.0–12.0 $g \cdot m^{-2}$). Above −23°C, IWP is no longer sensitive to temperature and remains in the range 8.0–10.0 $g \cdot m^{-2}$. For a given temperature ranging from −35°C to −23°C, an increase in IWP within 1.0–2.0 $g \cdot m^{-2}$ is obviously detected over the 30 years between P2 (1983–1992) and P3 (2013–2022).

The increase in in-cloud temperature from P1 to P4 is obvious from a maximum of −24°C in P1, −21°C in P2, −18°C in P3 to a maximum of −17°C in P4 (Figure 5c). Trends in 2-m temperatures at the Concordia station have already been studied based on several meteorological reanalyses (Ricaud et al., 2020b) over 50 years. Positive

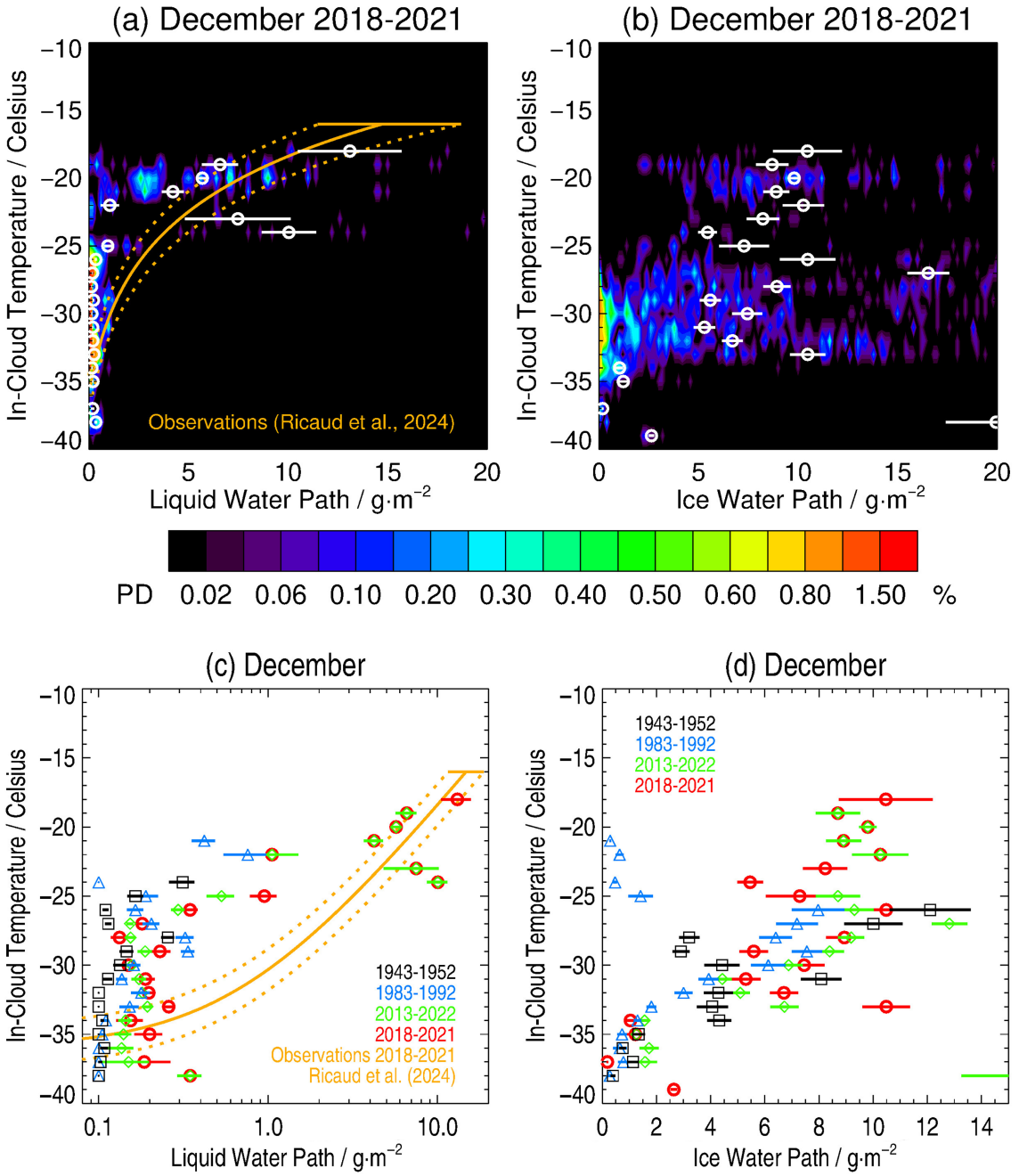

FIGURE 5 (a) Probability density (PD, %) of the in-cloud temperature (Celsius) as a function of liquid water path (LWP, g·m^{-2}) calculated from ERA5 reanalyses during December 2018–2021 at Concordia station, Antarctica. Also are represented the weighted-average LWPs within each 1-°C bin in temperature (white circles) with a horizontal bar showing the random error ($\pm\delta_{LWP}$) on the LWP mean. (b) Probability density (PD, %) of the in-cloud temperature (Celsius) as a function of ice water path (IWP, g·m^{-2}) calculated from ERA5 reanalyses during December 2018–2021 at Concordia station, Antarctica. Weighted-average IWPs within each 1-°C bin in temperature (white circles) are also represented, with a horizontal bar showing the random error ($\pm\delta_{IWP}$) of the IWP mean. (c) Weighted-average LWPs (g·m^{-2}) within each 1-°C bin in in-SLW cloud temperature with an horizontal bar showing the random error ($\pm\delta_{LWP}$) of the LWP mean calculated from ERA5 reanalyses at Concordia station, Antarctica during four periods: 1943–1952 (black squares, P1); 1983–1992 (blue triangles, P2); 2013–2022 (green diamonds, P3) and 2018–2021 (red circles, P4). (d) Weighted-average IWPs within each 1-°C bin in in-SLW (supercooled liquid water) cloud temperature with a horizontal bar showing the random error ($\pm\delta_{IWP}$) of the IWP mean calculated from ERA5 reanalyses at Concordia station, Antarctica during four periods: 1943–1952 (black squares, P1); 1983–1992 (blue triangles, P2); 2013–2022 (green diamonds, P3) and 2018–2021 (red circles, P4). A logarithmic function (orange solid) with its domain of validity (within the two dashed orange lines) derived from unbiased observations performed at Concordia station in P4 is superimposed in panels a and c. [Colour figure can be viewed at wileyonlinelibrary.com]

decadal trends were unambiguously stated during the summer season of December–January–February. But this evolution was correlated to the impact of the middle latitudes that affects the interior of the Antarctic Eastern Plateau through the Southern Annular Mode index providing warm air masses enriched in water vapour. One of the key signatures is the phenomenon known as atmospheric rivers (Wille et al., 2024a,b). As a consequence, increasing temperatures and water vapour enhance (1) the potential of SLW in cold clouds and (2) the SLW CRF at these high latitudes. Although the amount of SLW is weak, its impact on the Earth radiative balance is of a crucial importance and should be treated carefully to overcome the modelled deficit and quantify the climate evolution.

If we now consider the relationship between in-cloud temperature and LWC ($g{\cdot}m^{-3}$) and IWC ($g{\cdot}m^{-3}$) during the contemporary period P4 as presented in Figure 6a,b, respectively, there are mainly two domains. The first one is centred at −30°C from −25°C to −35°C and contains the majority of SLW clouds (Figure S7a) and ice water clouds (Figure S7b). The second one is fixed at higher temperatures at -20 ± 2°C and contains about 10% of the SLW and ice clouds. The domain encompassing -23 ± 1°C does not show significant SLW and ice clouds (<1%).

The time evolution of the presence of SLW and ice clouds from P1 to P4 is shown in Figure 6c,d, respectively. Whatever the period considered, the majority of SLW and ice clouds are always seen around −28°C to −32°C. But, for temperatures greater than −23°C, centred at -20 ± 1°C, there are no significant SLW or ice clouds in the periods P1 and P2. In other words, only one regime is depicted in the ERA5 dataset, contrarily with the P3 and P4 periods when two regimes are observed. To synthetise, and consistent with the results found with LWP and IWP, the contemporary periods P3 and P4 are the only periods when a significant amount of ice and SLW clouds is detected for temperatures greater than −23°C.

6.3 | Liquid fog

In a recent study focussing on the diurnal variation of the planetary boundary layer (PBL) top height impacting the presence of SLW clouds in summer over the Concordia station (Ricaud et al., 2025), three main points have been underlined. (1) The majority of SLW clouds were present in the entrainment zone and the capping inversion layer between 400 and 600 m agl from 0600 to 1400 UTC (from 14:00 to 22:00 local time [LT]) at the top height of the PBL. (2) The liquid fog within the stable boundary layer was essentially detected below 100 m agl during the very low temperature and high relative humidity period from 1800 to 0200 UTC (from 02:00 to 10:00 LT). LWPs associated with liquid fog periods are measured to be less than approximately $2\,g{\cdot}m^{-2}$ (Ricaud et al., 2024) that is consistent with observations performed in the Arctic winter with values less than approximately $5\,g{\cdot}m^{-2}$ (Cox et al., 2019). Note that, in the Arctic summer, LWPs are usually greater than approximately $20\,g{\cdot}m^{-2}$ (Guy et al., 2022; Miller et al., 2015; Shupe, 2011). (3) The SLW clouds may also be present in a layer named 'fossil layer' either advected via long-range transport or as a remnant of the PBL present over the station one or a few days earlier. The 'fossil layer' could be, by definition, detected at any height but statistically was present above the entrainment zone and the capping inversion layer in a domain from 600 to 900 m agl from 0000 to 2400 UTC.

We already noticed that the PBL top height from ERA5 is very consistent to within 20–30 m with the calculations from the ARPEGE numerical weather prediction (NWP) model and with the observations (Ricaud et al., 2025). Unfortunately, the vertical resolution of the ERA5 outputs (∼500 m) is certainly not high enough for showing up liquid fog in the very thin (< 100 m) stable boundary layer that develops between 1800 and 2400 UTC (02:00–08:00 LT). These later phenomena (liquid fog or SLW clouds) represent about 20%–30% of the SLW clouds present above Concordia over the period from 1800 to 2400 UTC. But whatever the surface elevation, the actual vertical resolution of the ERA5 L137 model is very high in the lowermost layers close to the surface with three layers between the surface and approximately 50 m agl and two more layers up to approximately 100 m agl (see https://confluence.ecmwf.int/display/UDOC/L137+model+level+definitions). This means that liquid fog may well be produced by the ERA5 model (see next Section) even if the conclusions derived from ERA5 liquid water clouds and satellite observations (Hellmuth et al., 2025) state that the representation of cloud microphysics in ERA5 should be refined to lessen ERA5 biases with observations.

6.4 | Diurnal variation

The diurnal variations of the percentage of SLW clouds calculated by ERA5 per vertical level at 650, 600, 550 and 500 hPa over the four periods P1 to P4 are displayed in Figure 7. Over the periods P1 (Figure 7a) and P2 (Figure 7b), the SLW clouds are mainly situated in the lowermost level at 650 hPa over 24 hours, with some slight exceptions at 1000–1400 UTC (18:00–22:00 LT) when SLW clouds might be present by 30%–40% at 550 hPa (P1) and 600 hPa (P2). In the contemporary era, over the periods P3 (Figure 7c) and P4 (Figure 7d), the percentage of SLW clouds in ERA5 notably changes, showing a pronounced

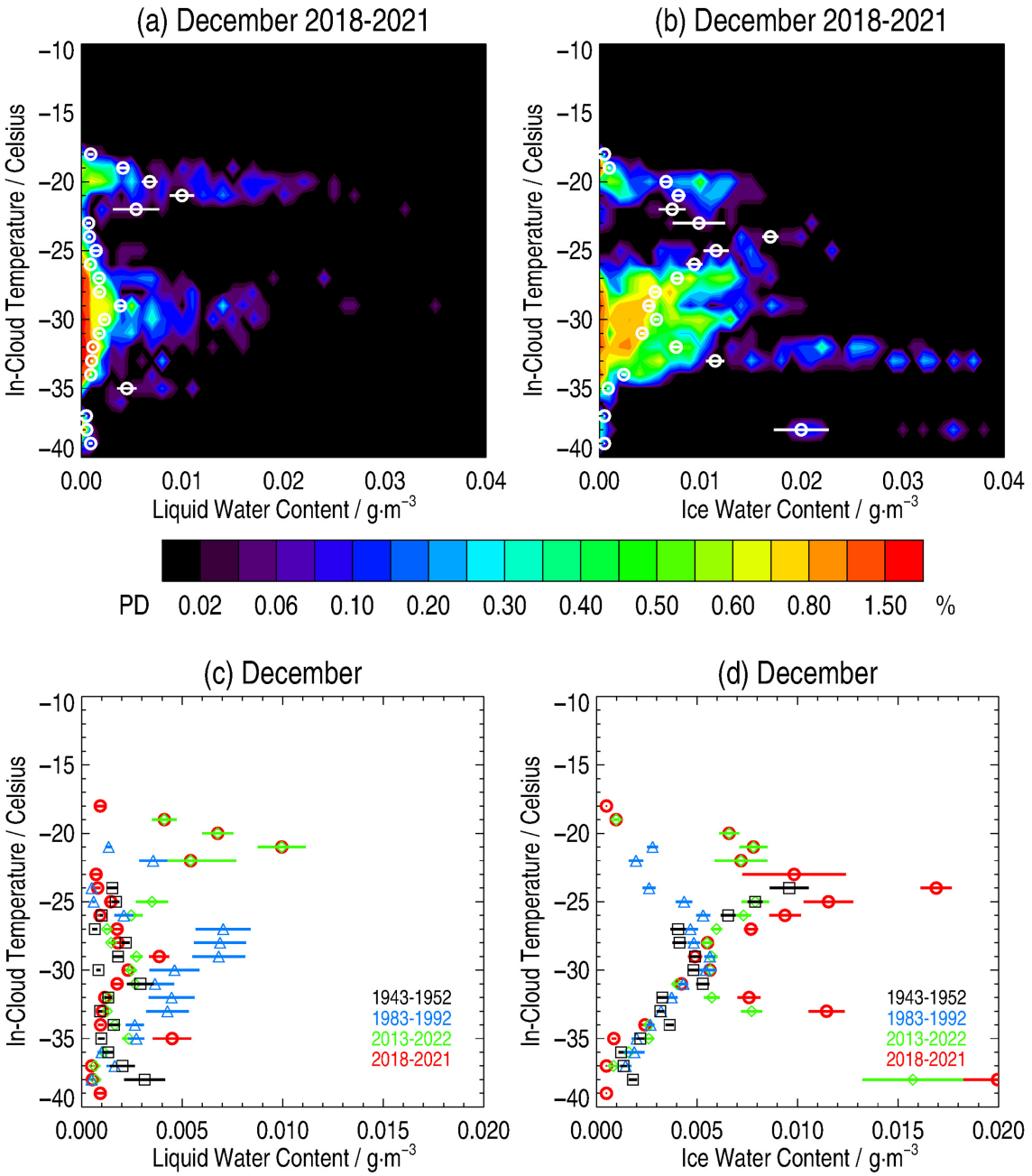

FIGURE 6 (a) Probability density (PD, %) of the in-cloud temperature (°Celsius) as a function of liquid water content (LWC, $g{\cdot}m^{-3}$) calculated from ERA5 reanalyses during December 2018–2021 at Concordia station, Antarctica. The weighted-average liquid water contents (LWCs) within each 1-°C bin in temperature (white circles) are also represented, with a horizontal bar showing the random error ($\pm\delta_{LWC}$) of the LWC mean. (b) Probability density (PD, %) of the in-cloud temperature (°Celsius) as a function of ice water content (IWC, $g{\cdot}m^{-3}$) calculated from ERA5 reanalyses during December 2018–2021 at Concordia station, Antarctica. The weighted-average IWCs within each 1-°C bin in temperature (white circles) are also represented, with a horizontal bar showing the random error ($\pm\delta_{IWC}$) of the IWC mean. (c) Weighted-average LWCs ($g{\cdot}m^{-3}$) within each 1-°C bin in in-SLW (supercooled liquid water) cloud temperature with an horizontal bar showing the random error ($\pm\delta_{LWC}$) on the LWC mean calculated from ERA5 reanalyses at Concordia station, Antarctica during four periods: 1943–1952 (black squares, P1); 1983–1992 (blue triangles, P2); 2013–2022 (green diamonds, P3) and 2018–2021 (red circles, P4). (d) Weighted-average IWCs within each 1-°C bin in in-SLW cloud temperature with a horizontal bar showing the random error ($\pm\delta_{IWC}$) of the IWC mean calculated from ERA5 reanalyses at Concordia station, Antarctica during four periods: 1943–1952 (black squares, P1); 1983–1992 (blue triangles, P2); 2013–2022 (green diamonds, P3) and 2018–2021 (red circles, P4). [Colour figure can be viewed at wileyonlinelibrary.com]

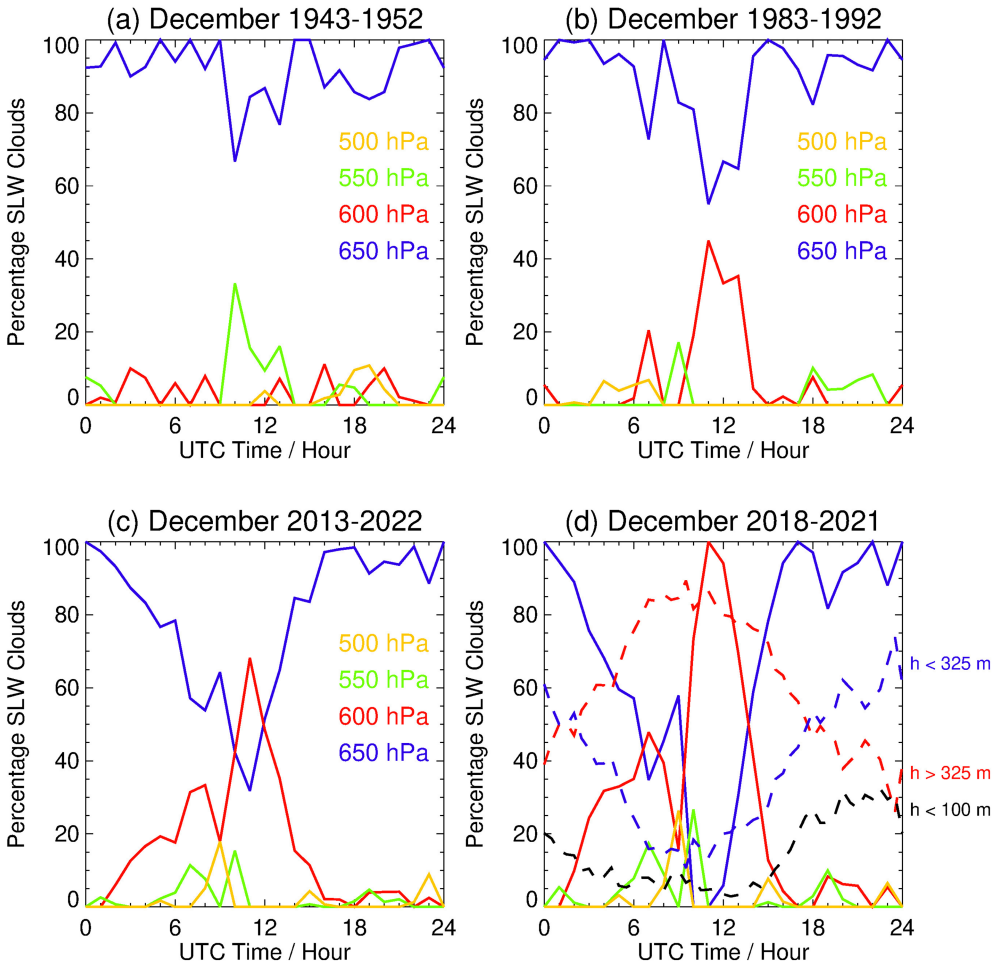

FIGURE 7 Diurnal variation of the percentage of supercooled liquid water (SLW) clouds calculated by ERA5 per vertical level at 650 (blue), 600 (red), 550 (green) and 500 hPa (orange) over the four December periods: (a) 1943–1952 (P1), (b) 1983–1992 (P2), (c) 2013–2022 (P3) and (d) 2018–2021 (P4). On panel d, we have inserted the statistics based on SLW cloud observations (Ricaud et al., 2025) during P4 below 325 m above ground level (agl) (blue dashed line), above 325 m agl (red dashed line) and below 100 m agl (black dashed line). [Colour figure can be viewed at wileyonlinelibrary.com]

diurnal change with SLW clouds present (more than 60% of occurrences) at 650 hPa from 1400 to 0600 UTC (from 22:00 to 14:00 LT) and at 600 hPa the remaining time, maximising at 1100–1200 UTC (19:00–20:00 LT) with an occurrence reaching 100% in P4. The results obtained during P4 (Figure 7d) with ERA5 data are remarkably consistent with the results obtained from observations (Ricaud et al., 2025) showing maxima at SLW clouds centred around 500 m agl from 0600 to 1400 UTC, with the remaining times SLW clouds observed from the surface to about 700 m agl. Note that, in the observations, surface-SLW clouds are mainly found from 1800 to 2400 UTC.

The comparisons between ERA5 in P4 (Figure 7d) and observations of the percentage SLW clouds at different layers are worth discussing. From Ricaud et al. (2025), the diurnal variation of the SLW cloud height is mainly driven by the clouds located above 325 m agl. Although the majority of SLW clouds are observed after 1200 UTC, clouds above 325 m agl are mostly (>60%) detected between 0600 and 1800 UTC while clouds below 100 m agl are mostly (>10%) detected between 1800 and 2400 UTC where liquid fog may occur. The heights of 100 and 325 m agl were empirically selected by analysing the climatological dataset. Above Concordia, in December 2018–2011 (period P4), the heights of 100 and 325 m agl correspond approximately to the pressure levels of 640 ± 2.0 and 620.0 ± 2.0 hPa, respectively. Therefore, the statistics based on the ERA5 data for the levels of 650 and 600 hPa coincide with the climatological study based on observations below 100 m agl and above 325 m agl, respectively.

From Figure 7d, in the lowermost layers (<325 m agl for the observations and at 650 hPa in ERA5), the percentage consistently minimises around 1100–1300 UTC (ERA5) and 0600–1500 UTC (observations), and conversely above (>325 m agl for the observations and at 600 hPa in ERA5). There is no sharp difference in the vertical distribution of the observed SLW clouds between 1800 and 2400 UTC, except very close to the surface (<100 m agl) where liquid fog may form. Because of the low vertical resolution of the ERA5 dataset outputs, the SLW clouds can be shown only at two levels (650 and 600 hPa) having a dominance of SLW clouds at 650 hPa (90%–100%) between 1800 and 2400 UTC. Since the PBL depth is so thin (30–100 m) within this period, we cannot rule out that ERA5 is actually able to calculate liquid fog between the

surface and the top of the PBL, highlighting SLW clouds in the lowermost level at 650 hPa.

The diurnal cycle of the SLW clouds in ERA5 becomes stronger over time. To quantify the main driver of this change, we have investigated the diurnal variation of the in-cloud temperature (Figure S8) and relative humidity (Figure S9) over the four periods (P1–P4) and over the four lowermost levels: 650, 600, 550 and 500 hPa. At 650 hPa (Figure S8), in-cloud temperatures in P1 and P2 appear to be slightly less than in P3 and P4 by 1–2°C, with a warmer period covering 1800–2400 UTC in P4. At 600 hPa, from 0800 to 1400 UTC, in-cloud temperatures in P3–P4 are much greater than in P1–P2 by 3–4°C. It is then difficult to attribute any change in the diurnal cycle of the SLW clouds over time to in-cloud temperature.

If we now consider the in-cloud relative humidity diurnal cycle over time (Figure S9), we can see the high correlation with the cycle of the SLW clouds. At 650 hPa, the relative humidity dramatically decreases in P3–P4 around 0800–1400 UTC (reaching 5%–40%) while in P1–P2 it is only 70%–80%. Conversely, at 600 hPa, the in-cloud relative humidity is at its maximum around 0800–1400 UTC in P3–P4 (60%–100%) with less intense values in P1–P2 (10–40%). The amplitude and the phase of the diurnal variation of the in-cloud relative humidity at 650 and 600 hPa are highly correlated with the diurnal variation of SLW cloud occurrences, explaining the greater sensitivity of the cycle in P3–P4 compared to P1–P2. Note that, at 500 and 550 hPa, the amplitude of the cycle (10%–20%) and the amount of in-cloud relative humidity (< 35%) do not favour the formation of SLW clouds. To conclude, relative humidity is the main driver to produce a diurnal cycle of the SLW clouds in ERA5 more intense with time.

7 | CONCLUSIONS

The present study aims at evaluating the ERA5 reanalyses over the Concordia station (Antarctica) focussing on the SLW clouds and their associated SLW CRF as a function of LWP following three main objectives. (1) The ERA5 datasets were confronted to published observations performed during four summer campaigns in December 2018–2021 and labelled as period P4. (2) We identified and assessed potential sources of bias in the ERA5 dataset. And (3) the time evolutions of SLW clouds and associated radiative forcing were studied over three other periods: December 1943–1952 (P1), 1983–1992 (P2), and 2013–2022 (P3). Note that P3 is encompassing P4.

We found that, during the contemporary era in line with observations (P4), the ERA5 distribution of SLW CRF–LWP conforms to the observational relationship and remains within its domain of validity. SLW CRF varies from 0 to a maximum of 55 $W \cdot m^{-2}$ when LWP varies from 0.1 to a maximum of 1.4 $g \cdot m^{-2}$. But the maximum of SLW CRF in ERA5 underestimates the observations by approximately −15 $W \cdot m^{-2}$ (∼20%) attributed to biases in long-wave downward SLW CRF (accounting for two-thirds of the deficit) and short-wave SLW CRF (one-third). Regarding the time evolutions of the SLW clouds and associated SLW CRF since the 1940s, we show that, with the positive trend in temperatures over 80 years (maximum in-cloud temperatures from −23°C in P1 to −18°C in P4), summertime SLW clouds are more present in the 2020s than in the 1940s.

Regarding the trends, we have to underline that the quality of the meteorological reanalyses at global scale prior to the 1980s is less than in the contemporary era. As a matter of fact, errors associated with ERA5 data are much larger in P1 than in P2. But we did not assess any trends in the ERA5 data between P1 and P2. Therefore, the positive trends in temperature and occurrence of the SLW clouds detected in the ERA5 dataset are mainly from the 1980s to the contemporary era over Concordia station and can be considered as a footprint of the evolution of Antarctic climate over 50 years.

As a general conclusion, consistent with numerous recent studies as, for example, Hellmuth et al. (2025), our study stresses the fact that SLW clouds and their associated SLW CRF should be treated in models with great attention to estimate the climate evolution over Antarctica and, more generally, at the global scale.

ACKNOWLEDGEMENTS

The permanently staffed Concordia station is jointly operated by the French Polar Institute (IPEV) and the Italian Programma Nazionale Ricerche in Antartide (PNRA). Finally, we would like to thank the three anonymous reviewers for their beneficial comments.

CONFLICT OF INTEREST STATEMENT

The author declares that he has no conflict of interest.

DATA AVAILABILITY STATEMENT

The data that support the findings of this study are available in ERA5 at https://cds.climate.copernicus.eu. These data were derived from the following resources available in the public domain: ERA5, https://cds.climate.copernicus.eu.

ORCID

Philippe Ricaud https://orcid.org/0000-0002-7133-1734

REFERENCES

Bell, B., Hersbach, H., Simmons, A., Berrisford, P., Dahlgren, P., Horányi, A. et al. (2021) The ERA5 global reanalysis: preliminary

extension to 1950. *Quarterly Journal of the Royal Meteorological Society*, 147(741), 4186–4227. Available from: https://doi.org/10.1002/qj.4174

Bergeron, T. (1928) Über die dreidimensional verknüpfende Wetteranalyse. *Geophysica Norvegica*, 5(6), 1–111.

Bevington, P. & Robinson, D.K. (2003) *Data reduction and error analysis for the physical sciences*. New York: McGraw-Hill Education, p. 320.

Bodas-Salcedo, A., Hill, P.G., Furtado, K., Williams, K.D., Field, P.R., Manners, J.C. et al. (2016) Large contribution of supercooled liquid clouds to the solar radiation budget of the Southern Ocean. *Journal of Climate*, 29(11), 4213–4228. Available from: https://doi.org/10.1175/jcli-d-15-0564.1

Bromwich, D.H., Nicolas, J.P., Hines, K.M., Kay, J.E., Key, E.L., Lazzara, M.A. et al. (2012) Tropospheric clouds in Antarctica. *Reviews of Geophysics*, 50, RG1004. Available from: https://doi.org/10.1029/2011RG000363

Bromwich, D.H., Otieno, F.O., Hines, K.M., Manning, K.W. & Shilo, E. (2013) Comprehensive evaluation of polar weather research and forecasting model performance in the Antarctic. *Journal of Geophysical Research-Atmospheres*, 118, 274–292.

Choi, Y.S., Ho, C.H., Park, C.E., Storelvmo, T. & Tan, I. (2014) Influence of cloud phase composition on climate feedbacks. *Journal of Geophysical Research: Atmospheres*, 119(7), 3687–3700. Available from: https://doi.org/10.1002/2013jd020582

Cossich, W., Maestri, T., Magurno, D., Martinazzo, M., Di Natale, G., Palchetti, L. et al. (2021) Ice and mixed-phase cloud statistics on the Antarctic plateau. *Atmospheric Chemistry and Physics*, 21, 13811–13833. Available from: https://doi.org/10.5194/acp-21-13811-2021

Cox, C.J., Noone, D.C., Berkelhammer, M., Shupe, M.D., Neff, W.D., Miller, N.B. et al. (2019) Supercooled liquid fogs over the central Greenland ice sheet. *Atmospheric Chemistry and Physics*, 19, 7467–7485. Available from: https://doi.org/10.5194/acp-19-7467-2019

Driemel, A., Augustine, J., Behrens, K., Colle, S., Cox, C., Cuevas-Agulló, E. et al. (2018) Baseline surface radiation network (BSRN): structure and data description (1992–2017). *Earth System Science Data*, 10, 1491–1501. Available from: https://doi.org/10.5194/essd-10-1491-2018

Dupont, J.C., Haeffelin, M., Drobinski, P. & Besnard, T. (2008) Parametric model to estimate clear-sky longwave irradiance at the surface on the basis of vertical distribution of humidity and temperature. *Journal of Geophysical Research-Atmospheres*, 113, D07203. Available from: https://doi.org/10.1029/2007JD009046

Dutton, E.G., Farhadi, A., Stone, R.S., Long, C.N. & Nelson, D.W. (2004) Long-term variations in the occurrence and effective solar transmission of clouds as determined from surface-based total irradiance observations. *Journal of Geophysical Research: Atmospheres*, 109(D3), D03204. Available from: https://doi.org/10.1029/2003JD003568

Findeisen, W. (1938) Kolloid-meteorologische Vorgänge bei Niederschlagsbildung. *Meteorologische Zeitschrift*, 55, 121–133.

Forbes, R.M. & Ahlgrimm, M. (2014) On the representation of high-latitude boundary layer mixed-phase cloud in the ECMWF global model. *Monthly Weather Review*, 142(9), 3425–3445.

Gardner, A.S. & Sharp, M.J. (2010) A review of snow and ice albedo and the development of a new physically based broadband albedo parameterization. *Journal of Geophysical Research: Earth Surface*, 115(F1): 1–15.

Goy, C., Potenza, M.A., Dedera, S., Tomut, M., Guillerm, E., Kalinin, A. et al. (2018) Shrinking of rapidly evaporating water microdroplets reveals their extreme supercooling. *Physical Review Letters*, 120, 015501. Available from: https://doi.org/10.1103/PhysRevLett.120.015501

Grosvenor, D.P., Choularton, T.W., Lachlan-Cope, T., Gallagher, M.W., Crosier, J., Bower, K.N. et al. (2012) In-situ aircraft observations of ice concentrations within clouds over the Antarctic peninsula and Larsen ice shelf. *Atmospheric Chemistry and Physics*, 12, 11275–11294. Available from: https://doi.org/10.5194/acp-12-11275-2012

Guy, H., Turner, D.D., Walden, V.P., Brooks, I.M. & Neely, R.R. (2022) Passive ground-based remote sensing of radiation fog. *Atmospheric Measurement Techniques*, 15, 5095–5115. Available from: https://doi.org/10.5194/amt-15-5095-2022

Hellmuth, F., Carlsen, T., Daloz, A.S., David, R.O., Che, H. & Storelvmo, T. (2025) Evaluation of biases in mid-to-high-latitude surface snowfall and cloud phase in ERA5 and CMIP6 using satellite observations. *Atmospheric Chemistry and Physics*, 25(2), 1353–1383. Available from: https://doi.org/10.5194/acp-25-1353-2025

Hersbach, H., Bell, B., Berrisford, P., Hirahara, S., Horányi, A., Muñoz-Sabater, J. et al. (2020) The ERA5 global reanalysis. *Quarterly Journal of the Royal Meteorological Society*, 146(730), 1999–2049.

King, J.C., Argentini, S.A. & Anderson, P.S. (2006) Contrasts between the summertime surface energy balance and boundary layer structure at dome C and Halley stations, Antarctica. *Journal of Geophysical Research: Atmospheres*, 111, D02105. Available from: https://doi.org/10.1029/2005JD006130

King, J.C., Gadian, A., Kirchgaessner, A., Kuipers Munneke, P., Lachlan-Cope, T.A., Orr, A. et al. (2015) Validation of the summertime surface energy budget of Larsen C ice shelf (Antarctica) as represented in three high-resolution atmospheric models. *Journal of Geophysical Research-Atmospheres*, 120, 1335–1347. Available from: https://doi.org/10.1002/2014JD022604

Komurcu, M., Storelvmo, T., Tan, I., Lohmann, U., Yun, Y., Penner, J.E. et al. (2014) Intercomparison of the cloud water phase among global climate models. *Journal of Geophysical Research: Atmospheres*, 119(6), 3372–3400. Available from: https://doi.org/10.1002/2013jd021119

Lachlan-Cope, T. (2010) Antarctic clouds. *Polar Research*, 29, 150–158.

Lachlan-Cope, T., Listowski, C. & O'Shea, S. (2016) The microphysics of clouds over the Antarctic peninsula – part 1: observations. *Atmospheric Chemistry and Physics*, 16, 15605–15617. Available from: https://doi.org/10.5194/acp-16-15605-2016

Lawson, R.P. & Gettelman, A. (2014) Impact of Antarctic mixed-phase clouds on climate. *Proceedings of the National Academy of Sciences of the United States of America*, 111, 18156–18161.

Lemus, L., Rikus, L., Martin, C. & Platt, R. (1997) Global cloud liquid water path simulations. *Journal of Climate*, 10(1), 52–64.

Lenaerts, J.T., Van Tricht, K., Lhermitte, S. & L'Ecuyer, T.S. (2017) Polar clouds and radiation in satellite observations, reanalyses, and climate models. *Geophysical Research Letters*, 44(7), 3355–3364.

Listowski, C., Delanoë, J., Kirchgaessner, A., Lachlan-Cope, T. & King, J. (2019) Antarctic clouds, supercooled liquid water and mixed phase, investigated with DARDAR: geographical

and seasonal variations. *Atmospheric Chemistry and Physics*, 19, 6771–6808. Available from: https://doi.org/10.5194/acp-19-6771-2019

Listowski, C. & Lachlan-Cope, T. (2017) The microphysics of clouds over the Antarctic peninsula – part 2: modelling aspects within polar WRF. *Atmospheric Chemistry and Physics*, 17, 10195–10221. Available from: https://doi.org/10.5194/acp-17-10195-2017

Lubin, D., Chen, B., Bromwich, D.H., Somerville, R.C., Lee, W.H. & Hines, K.M. (1998) The impact of Antarctic cloud radiative properties on a GCM climate simulation. *Journal of Climate*, 11, 447–462.

McCoy, D.T., Hartmann, D.L., Zelinka, M.D., Ceppi, P. & Grosvenor, D.P. (2015) Mixed-phase cloud physics and Southern Ocean cloud feedback in climate models. *Journal of Geophysical Research: Atmospheres*, 120(18), 9539–9554. Available from: https://doi.org/10.1002/2015jd023603

Miller, N.B., Shupe, M.D., Cox, C.J., Walden, V.P., Turner, D.D. & Steffen, K. (2015) Cloud radiative forcing at summit, Greenland. *Journal of Climate*, 28(15), 6267–6280. Available from: https://doi.org/10.1175/JCLI-D-15-0076.1

Ricaud, P., Del Guasta, M., Bazile, E., Azouz, N., Lupi, A., Durand, P. et al. (2020a) Supercooled liquid water cloud observed, analysed, and modelled at the top of the planetary boundary layer above dome C, Antarctica. *Atmospheric Chemistry and Physics*, 20, 4167–4191. Available from: https://doi.org/10.5194/acp-20-4167-2020

Ricaud, P., Del Guasta, M., Lupi, A., Roehrig, R., Bazile, E., Durand, P. et al. (2024) Supercooled liquid water clouds observed over dome C, Antarctica: temperature sensitivity and cloud radiative forcing. *Atmospheric Chemistry and Physics*, 24, 613–630. Available from: https://doi.org/10.5194/acp-24-613-2024

Ricaud, P., Durand, P., Grigioni, P., Ciardini, V., Del Guasta, M., Camporeale, G. et al. (2025) Diurnal variation of the planetary boundary layer over dome C (Antarctica) impacting the formation of supercooled liquid water clouds. *Polar Science*, 101256. Available from: https://doi.org/10.1016/j.polar.2025.101256

Ricaud, P., Grigioni, P., Roehrig, R., Durand, P. & Veron, D.E. (2020b) Trends in atmospheric humidity and temperature above dome C, Antarctica evaluated from observations and Reanalyses. *Atmosphere*, 11, 836. Available from: https://doi.org/10.3390/atmos11080836

Ricaud, P., Medina, P., Durand, P., Attié, J.L., Bazile, E., Grigioni, P. et al. (2023) In situ VTOL drone-borne observations of temperature and relative humidity over dome C, Antarctica. *Drones*, 7(8), 532. Available from: https://doi.org/10.3390/drones7080532

Shupe, M.D. (2011) Clouds at Arctic atmospheric observatories. Part II: thermodynamic phase characteristics. *Journal of Applied Meteorology and Climatology*, 50(3), 645–661. Available from: https://doi.org/10.1175/2010JAMC2468.1

Silber, I., Verlinde, J., Cadeddu, M., Flynn, C.J., Vogelmann, A.M. & Eloranta, E.W. (2019b) Antarctic cloud macrophysical, thermodynamic phase, and atmospheric inversion coupling properties at McMurdo Station—part II: radiative impact during different synoptic regimes. *Journal of Geophysical Research: Atmospheres*, 124, 1697–1719. Available from: https://doi.org/10.1029/2018JD029471

Silber, I., Verlinde, J., Wang, S.H., Bromwich, D.H., Fridlind, A.M., Cadeddu, M. et al. (2019a) Cloud influence on ERA5 and AMPS surface downwelling longwave radiation biases in West Antarctica. *Journal of Climate*, 32(22), 7935–7949. Available from: https://doi.org/10.1175/JCLI-D-19-0149.1

Sippola, H. & Taskinen, P. (2018) Activity of supercooled water on the ice curve and other thermodynamic properties of liquid water up to the boiling point at standard pressure. *Journal of Chemical and Engineering Data*, 63(8), 2986–2998.

Soci, C., Hersbach, H., Simmons, A., Poli, P., Bell, B., Berrisford, P. et al. (2024) The ERA5 global reanalysis from 1940 to 2022. *Quarterly Journal of the Royal Meteorological Society*, 150(764), 4014–4048. Available from: https://doi.org/10.1002/qj.4803

Stapf, J., Ehrlich, A., Jäkel, E., Lüpkes, C. & Wendisch, M. (2020) Reassessment of shortwave surface cloud radiative forcing in the Arctic: consideration of surface-albedo–cloud interactions. *Atmospheric Chemistry and Physics*, 20, 9895–9914. Available from: https://doi.org/10.5194/acp-20-9895-2020

Storelvmo, T. (2017) Aerosol effects on climate via mixed-phase and ice clouds. *Annual Review of Earth and Planetary Sciences*, 45, 199–222. Available from: https://doi.org/10.1146/annurev-earth-060115-012240

Storelvmo, T. & Tan, I. (2015) The Wegener–Bergeron–Findeisen process—its discovery and vital importance for weather and climate. *Meteorologische Zeitschrift*, 24, 455–461.

Tetzner, D., Thomas, E. & Allen, C. (2019) A validation of ERA5 reanalysis data in the southern Antarctic peninsula—Ellsworth Land region, and its implications for ice Core studies. *Geosciences*, 9, 289. Available from: https://doi.org/10.3390/geosciences9070289

Tsushima, Y., Emori, S., Ogura, T., Kimoto, M., Webb, M.J., Williams, K.D. et al. (2006) Importance of the mixed-phase cloud distribution in the control climate for assessing the response of clouds to carbon dioxide increase: a multi-model study. *Climate Dynamics*, 27(2), 113–126. Available from: https://doi.org/10.1007/s00382-006-0127-7

Turner, D.D., Vogelmann, A.M., Austin, R.T., Barnard, J.C., Cady-Pereira, K., Chiu, J.C. et al. (2007) Thin liquid water clouds: their importance and our challenge. *Bulletin of the American Meteorological Society*, 88(2), 177–190. Available from: https://doi.org/10.1175/BAMS-88-2-177

Wang, Y., Li, J., Zhao, Y., Li, Y., Zhao, Y. & Wu, X. (2022) Distinct diurnal cycle of supercooled water cloud fraction dominated by dust extinction coefficient. *Geophysical Research Letters*, 49, e2021GL097006. Available from: https://doi.org/10.1029/2021GL097006

Wegener, A. (1911) *Thermodynamik der Atmosphäre*. Leipzig, Germany: Barth.

Wille, J.D., Alexander, S.P., Amory, C., Baiman, R., Barthélemy, L., Bergstrom, D.M. et al. (2024b) The extraordinary march 2022 East Antarctica "heat" wave. part II: impacts on the Antarctic ice sheet. *Journal of Climate*, 37(3), 779–799. Available from: https://doi.org/10.1175/JCLI-D-23-0176.1

Wille, J.D., Alexander, S.P., Amory, C., Baiman, R., Barthélemy, L., Bergstrom, D.M. et al. (2024a) The extraordinary march 2022 East Antarctica heat wave. part I: observations and meteorological drivers. *Journal of Climate*, 37(3), 757–778. Available from: https://doi.org/10.1175/JCLI-D-23-0175.1

Young, G., Lachlan-Cope, T., O'Shea, S.J., Dearden, C., Listowski, C., Bower, K.N. et al. (2019) Radiative effects of secondary ice

enhancement in coastal Antarctic clouds. *Geophysical Research Letters*, 46, 2312–2321. Available from: https://doi.org/10.1029/2018GL080551

Zhang, D., Vogelmann, A., Kollias, P., Luke, E., Yang, F., Lubin, D. et al. (2019) Comparison of Antarctic and Arctic single-layer stratiform mixed-phase cloud properties using ground-based remote sensing measurements. *Journal of Geophysical Research: Atmospheres*, 124(17–18), 10186–10204. Available from: https://doi.org/10.1029/2019JD030673

Zhu, J., Xie, A., Qin, X., Wang, Y., Xu, B. & Wang, Y. (2021) An assessment of ERA5 reanalysis for Antarctic near-surface air temperature. *Atmosphere*, 12(2), 217. Available from: https://doi.org/10.3390/atmos12020217

SUPPORTING INFORMATION

Additional supporting information can be found online in the Supporting Information section at the end of this article.

How to cite this article: Ricaud, P. (2025) ERA5 deficit in supercooled liquid water cloud radiative forcing at Dome C, Antarctica. *Quarterly Journal of the Royal Meteorological Society*, e70025. Available from: https://doi.org/10.1002/qj.70025